Atomic Structure of Amorphous Fe-Tb- and Amorphous Fe-Co-Tb-Alloys by Means of EDXD

R. Utz, A. Brunsch*, P. Lamparter, and S. Steeb
Max-Planck-Institut für Metallforschung, Institut für Werkstoffwissenschaft, Stuttgart

Z. Naturforsch. **44a**, 1201–1209 (1989); received September 23, 1989

We present structural investigations using the energy dispersive X-ray diffraction (EDXD)-method on amorphous Fe-Tb- and Fe-Co-Tb-alloys over an extended concentration range. Atomic distances, partial coordination numbers, and chemical short range order parameters are reported. The short range order is characterized by a compound forming tendency. In an amorphous Fe-Co-Tb-alloy, doping with hydrogen affects the short range order and gives rise to an in-plane magnetization direction.

1. Introduction

X-ray wide angle experiments are conventionally performed using the angular dispersive method (ADXD). In the present work we applied the energy dispersive X-ray diffraction method (EDXD) to the structural investigation of amorphous materials. This method was already applied to study crystalline [1] and non-crystalline materials [2, 3].

With the EDXD-method, the primary beam contains the continuous spectrum and the diffracted radiation is detected by a solid state energy-sensitive detector arranged at a fixed scattering angle 2Θ.

The advantage of this method is that structural information is obtained up to a large momentum transfer $Q = 4\pi(\sin\Theta)/\lambda$, where λ is the wavelength of the radiation. In real space this results in a high resolution around the first maximum of the atomic distribution function. This is of particular advantage for the investigation of such binary amorphous alloys where the atomic diameters of both components are rather different. This is the case for iron and terbium with atomic diameters of 2.48 Å and 3.52 Å, respectively.

Amorphous iron-rich Fe-Tb- and Fe-Co-Tb-alloys have gained appreciable importance by their possible application in the field of magneto-optical memory devices [4, 5]. They can be produced in a wide concentration range by sputtering. Furthermore it is possible to produce the Tb-rich alloys by the melt-spin-process.

In the present work the structure of amorphous Fe-(Co-)-Tb-alloys was studied. Furthermore we tried to find out whether the magnetic anisotropy is caused by a structural anisotropy.

2. Theoretical

2.1. Total Structure Factor and Total Pair Correlation Function

The total structure factor $S(Q)$ according to Faber-Ziman [6] follows from the coherently scattered intensity per atom $I_A(Q)$:

$$S(Q) = \frac{I_A(Q) - [\langle f(Q)^2\rangle - \langle f(Q)\rangle^2]}{\langle f(Q)\rangle^2} \tag{1}$$

with

$f_i(Q)$ = atomic scattering amplitude of component i,

$\langle f(Q)^2\rangle = \sum_{i=1}^{n} c_i f_i^2$,

$\langle f(Q)\rangle = \sum_{i=1}^{n} c_i f_i$,

c_i = atomic fraction of component i,

n = number of components forming the alloy.

From $S(Q)$ one obtains the total pair correlation function

$$G(R) = \frac{2}{\pi} R \int_0^\infty Q^2 [S(Q) - 1] \frac{\sin(QR)}{QR} \mathrm{d}Q, \tag{2}$$

where R = distance in real space.

---

* IBM Germany, German Manufacturing Technology Center, 7032 Sindelfingen.

Reprint requests to Prof. Dr. S. Steeb, Max-Planck-Institut für Metallforschung, Institut für Werkstoffwissenschaft, Seestraße 92, D-7000 Stuttgart 1.

0932-0784 / 89 / 1200-1201 $ 01.30/0. – Please order a reprint rather than making your own copy.

For a binary alloy, this total function can be represented by the three partial functions $G_{11}(R)$, $G_{22}(R)$, and $G_{12}(R)$

$$G(R) = \frac{c_1^2 f_1^2}{\langle f \rangle^2} G_{11}(R) + \frac{c_2^2 f_2^2}{\langle f \rangle^2} G_{22}(R) + \frac{2 c_1 c_2 f_1 f_2}{\langle f \rangle^2} G_{12}(R). \tag{3}$$

The weighting factors W_{ij} connected with the three G_{ij} thus apparently depend on the concentrations and on the scattering lengths.

$G(R)$ finally yields the pair distribution function $g(R)$

$$g(R) = \frac{G(R)}{4\pi \varrho_0 R} + 1 \tag{4}$$

with ϱ_0 = mean atomic number density.

The number of atoms in a spherical shell with radii between $R_i - \frac{1}{2}\Delta R$ and $R_i + \frac{1}{2}\Delta R$ amounts to

$$N(R_i) = \int_{R_i - \frac{\Delta R}{2}}^{R_i + \frac{\Delta R}{2}} 4\pi R^2 \varrho_0 \, g(R) \, \mathrm{d}R. \tag{5}$$

The total coordination number N can be represented for a binary alloy by three partial coordination numbers Z_{ij}:

$$\begin{aligned} N &= \frac{c_1 f_1^2}{\langle f \rangle^2} Z_{11} + \frac{c_2 f_2^2}{\langle f \rangle^2} Z_{22} + \frac{2 c_1 f_1 f_2}{\langle f \rangle^2} Z_{12} \\ &= N_{11} \qquad + N_{22} \qquad + N_{12}. \end{aligned} \tag{6}$$

To obtain the atomic distances and partial coordination numbers from a maximum in $g(R)$ which is splitted up into subpeaks, Gaussians of the form

$$F(R) = F_0 \exp\left[-\frac{(R - R_i)^2}{2\sigma^2} \right] \tag{7}$$

were used. R_i marks the position of a subpeak and σ the distance between R_i and the points of inflection. Fitting a function $F(R)$ to a subpeak in $g(R)$ yields the partial coordination number Z_{ij}:

$$Z_{ij} = N_{ij} \frac{\langle f \rangle^2}{c_i f_i f_j} = \left[4\pi \varrho_0 \int_0^\infty R^2 \cdot F(R) \cdot \mathrm{d}R \right] \frac{\langle f \rangle^2}{c_i f_i f_j}. \tag{8}$$

Partial coordination numbers can be used to calculate chemical short range order parameters which are a measure for the extent of short range order. Substances composed of two components A and B with different atomic diameters are described by the short range order parameter η_{AB} according to [7]:

$$\eta_{AB} = \frac{Z_{AB} \langle Z \rangle}{c_A Z_A Z_B} - 1 \tag{9}$$

with

Z_{AB} = number of B-atoms around an A-atom,
$Z_A = Z_{AA} + Z_{AB}$,
$Z_B = Z_{BB} + Z_{AB} \cdot \frac{c_A}{c_B}$,
$\langle Z \rangle = c_A Z_A + c_B Z_B$.

The normalized short range order parameter η^0_{AB} is defined as

$$\eta^0_{AB} = \frac{\eta_{AB}}{\eta^{\max}_{AB}} = \eta_{AB} \frac{c_B Z_B}{c_A Z_A} \quad \text{for} \quad c_A Z_A < c_B Z_B. \tag{10}$$

For statistical distribution of the atoms of both components one has $\eta^0_{AB} = 0$, for maximum compound formation $\eta^0_{AB} = 1$, and for maximum segregation $\eta^0_{AB} = -1$.

2.2. *EDXD-Method*

The intensity $I_{\exp}(E, \Theta)$ scattered from the specimen is composed of a coherent and an incoherent contribution:

$$\begin{aligned} I_{\exp}(E, \Theta) = {} & C\,\varepsilon(E) \\ & \cdot \left(I_0(E)\, P(E, \Theta)\, A(E, \Theta)\, [I_A + I^{ms}_{coh}]_{E,\Theta} \right. \\ & \left. + I_0(E')\, P(E, E', \Theta)\, A(E, E', \Theta)\, [I_{inc} + I^{ms}_{inc}]_{E',\Theta} \right) \end{aligned} \tag{11}$$

with

C = normalization constant,
$\varepsilon(E)$ = detector efficiency,
$I_0(E)$ = intensity of the primary spectrum,
$P(E, \Theta)$ = polarization correction,
$A(E, \Theta)$ = absorption correction,
$I_A(E, \Theta)$ = coherent single scattering intensity per atom,
I^{ms}_{coh} = coherent multiple scattering intensity per atom,
I^{ms}_{inc} = incoherent multiple scattering intensity per atom,
$I_{inc}(E', \Theta)$ = incoherent single scattering intensity per atom (Compton-scattering),
E' = original energy of the X-ray photon which is reduced by the Compton-effect to the energy E:

$$E' = E + \Delta E = \frac{E}{1 - 0.00391\, E \sin^2 \Theta}.$$

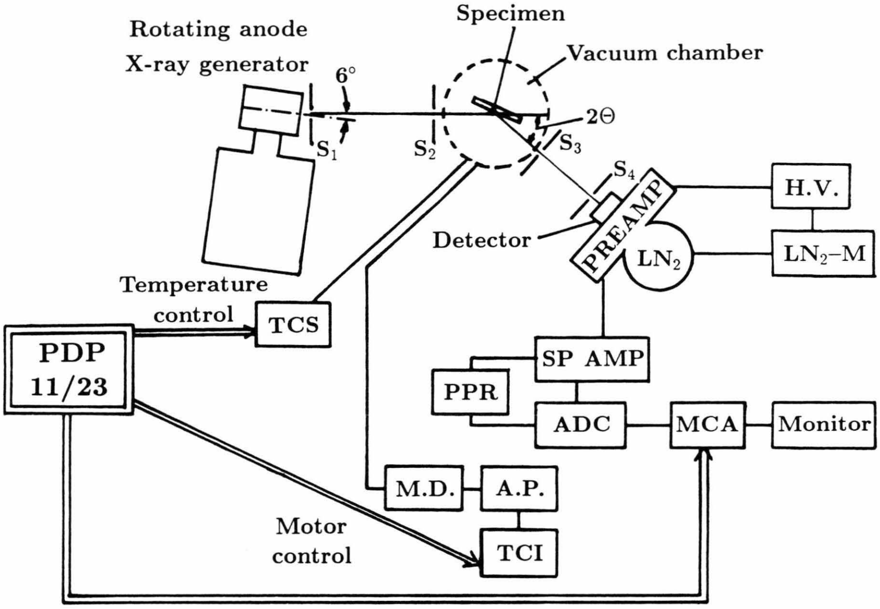

Fig. 1. EDXD-apparatus. Schematic diagram (see text).

Concerning a comprehensive discussion of all these terms and their determination during the evaluation procedure we refer to [8].

Finally, the structure factor $S(Q)$ is obtained from (1) and (11) using

$$Q = (4\pi/h\,c)\,E \sin\Theta\,, \tag{12}$$

h = Planck's constant, c = light velocity.

3. Experimental

3.1. EDXD-Apparatus and Experimental Procedure

Figure 1 shows a schematic diagram of the experimental set up. The X-rays produced on an Au-anode within a rotating anode X-ray generator (Rigaku RU-200; 12 kW) pass the slits S_1 and S_2 and then are scattered at the specimen which is placed in a vacuum chamber. The diffracted beam reaches the Si(Li)-detector through the slits S_3 and S_4. The detector and the preamplifier (PREAMP) are cooled by liquid nitrogen (LN_2) controlled by a monitor (LN_2-M). The intensities measured at a fixed angle are stored by a multichannel analyzer (MCA) as $I(E)$-presentation. For this procedure one needs a spectroscopy amplifier (SP AMP), a pulse pile up rejector (PPR), and an analog-digital converter (ADC). A computer (PDP 11/23) controls the MCA and the motor drive (M.D.) of the specimen rotation via an axis positioner (A.P.) and a telecomputer interface (TCI). For performing relaxation- and crystallization-experiments, a furnace with a temperature control system (TCS) is installed.

The useful energy range is limited experimentally by the following facts:

i) The characteristic radiation of the anode material and the Fe-fluorescence radiation of the specimen occur at energies <15 keV which therefore must be excluded from the evaluation procedure.

ii) The energies >40 keV have to be excluded since in that range the detector efficiency decreases strongly and since Tb-fluorescence radiation occurs. Thus for the Fe-Tb- and the Fe-Co-Tb-alloys an energy window between 18 keV and 38 keV was chosen for data evaluation. This limitation in the energy range means that for a distinct 2Θ-angle only a limited Q-range can be evaluated according to (12). Thus, for the determination of $S(Q)$ for an extended Q-range measurements at different 2Θ-angles are necessary. Figure 2 shows the choice of seven 2Θ-values used for the present measurements. Figure 3 shows as an example the intensity scattered at $2\Theta = 15°$ versus energy.

3.2. Specimen Preparation

In the present work, melt spun amorphous $Fe_{28}Tb_{72}$- and $Fe_{40}Tb_{60}$-alloys were investigated as well as amor-

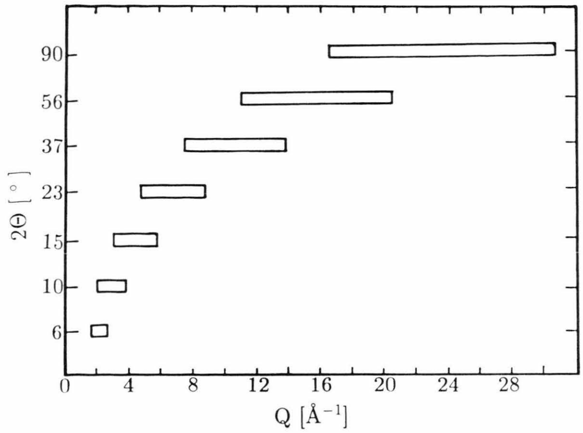

Fig. 2. Choice of 2Θ-angles to cover the Q-region up to 30 Å^{-1}.

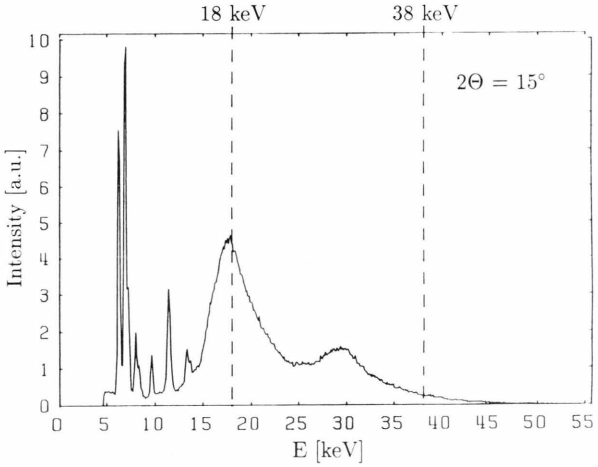

Fig. 3. Amorphous $Fe_{39}Tb_{61}$; $2\Theta = 15°$; measured intensity.

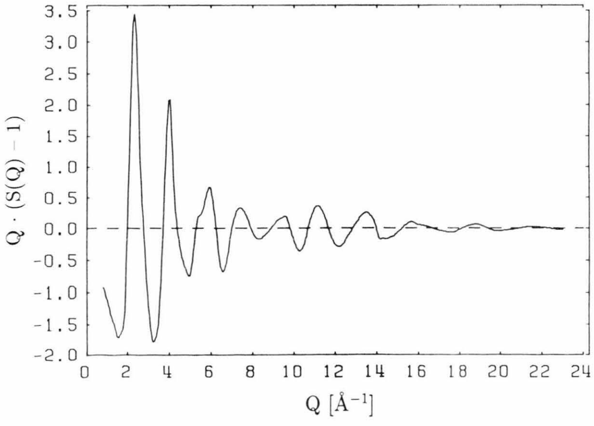

Fig. 4. Amorphous $Fe_{39}Tb_{61}$; $Q \cdot (S(Q) - 1)$; EDXD-method.

phous sputtered Fe_xTb_{100-x}-alloys ($x = 13$, 18, 21, 28, 39, 49, 63, 71, 75, and 80). To obtain these different concentrations, an Fe-Tb-target and a pure Tb-target were used simultaneously, which yielded on the substrate a sequence of specimen material with rising Fe-concentration depending on the different distances of the substrate points from the two targets. The concentrations were determined by electron microprobe [9]. The amorphous $Fe_{72}Co_8Tb_{20}$-, $Fe_{69}Co_{8.5}Tb_{22.5}$-, and $Fe_{68}Co_9Tb_{23}$-alloys were prepared by sputtering from targets which were produced in the first and second case by vacuum-melting and in the third case by plasma spraying in ($Ar + H_2$)-atmosphere. The determination of magnetic properties using a vibrating sample-magnetometer showed the axis of easy magnetization in the first two cases to be perpendicular to the specimen plane, and in the third case lying in the plane.

4. Results and Discussion

4.1. Amorphous Fe-Tb-Alloys

4.1.1. Structure Factors

Figure 4 shows the $Q \cdot (S(Q) - 1)$-function as obtained with amorphous $Fe_{39}Tb_{61}$ using the EDXD-method. It shows pronounced oscillations up to 24 Å^{-1}, whereas for ADXD-measurements the largest Q-value is normally 14 Å^{-1} and therefore with the ADXD-method the oscillations between 14 Å^{-1} and 24 Å^{-1} are not detected.

Figure 5 shows for eleven values of x the structure factors as obtained with amorphous Fe_xTb_{100-x}-alloys. Since the structure factors for $Q > 10$ Å^{-1} show only rather weak oscillations, only the region between 0 and 10 Å^{-1} is presented in Figure 5. However, it should be emphasized that all structure factors were measured up to 25 Å^{-1} and that the oscillations in the region $Q > 10$ Å^{-1} are very important to obtain a good resolution in R-space. The first maximum in Fig. 5 is shifted to larger Q-values for increasing Fe-concentration. This is in agreement with the fact that the diameter of the Fe-atom with 2.48 Å is smaller than that of the Tb-atom with 3.52 Å. Furthermore we observe for $x = 13$, 18, and 21 the occurrence of crystalline peaks. For large x-values the half width of the first maximum amounts to 0.75 Å^{-1}, which is much larger than the one observed in metal-metalloid alloys ($\Delta Q \sim 0.5$ Å^{-1}) [10]. The intensity of the second maximum decreases with increasing x.

Table 1. Position, height, and half width of the first peak of $S(Q)$. SP and MS mean specimen preparation by sputtering and melt spinning, respectively.

Specimen	First peak in $S(Q)$		
	Position Q_p [Å^{-1}]	Height	Half width ΔQ [Å^{-1}]
$Fe_{13}Tb_{87}$(SP)	2.26	5.26	0.23
$Fe_{18}Tb_{82}$(SP)	2.26	5.20	0.15
$Fe_{21}Tb_{79}$(SP)	2.26	3.82	0.23
$Fe_{28}Tb_{72}$(SP)	2.25	2.90	0.44
$Fe_{28}Tb_{72}$(MS)	2.26	2.81	0.42
$Fe_{39}Tb_{61}$(SP)	2.30	2.45	0.51
$Fe_{40}Tb_{60}$(MS)	2.30	2.66	0.42
$Fe_{49}Tb_{51}$(SP)	2.41	2.11	0.70
$Fe_{63}Tb_{37}$(SP)	2.58	2.07	0.75
$Fe_{71}Tb_{29}$(SP)	2.67	2.08	0.75
$Fe_{75}Tb_{25}$(SP)	2.76	2.12	0.74
$Fe_{78}Tb_{22}$(SP)	2.81	2.17	0.74
$Fe_{80}Tb_{20}$(SP)	2.85	2.18	0.78
$Fe_{72}Co_8Tb_{20}$(SP)	2.88	2.28	0.72
$Fe_{69}Co_{8.5}Tb_{22.5}$(SP)	2.85	2.25	0.70
$Fe_{68}Co_9Tb_{23}$(SP)			
$M_{1\parallel}$ } subpeaks of the	2.15	1.21	–
$M_{2\parallel}$ } first maximum	2.99	1.80	–

In Table 1 we show the position, height and half width of the first maximum in $S(Q)$ obtained with the specimens investigated during the present work.

4.1.2. Pair Correlation Functions

Figure 6 shows the $G(R)$-functions for the same Fe-concentrations as in Figure 5. The oscillations for $R > 6$ Å are strongly damped for the specimens with $x > 21$, which means that there are no long range correlations. The samples with $x = 13$ and 18 show microcrystalline regions, whereas for $x > 21$ the substances are fully amorphous. The structure of the $Fe_{21}Tb_{79}$-alloy lies in between the crystalline and the amorphous state.

4.1.2.1. Atomic Distances

As explained in Section 2.1, the atomic distances and partial coordination numbers can be obtained from Gaussian fitting to the first maximum in $g(R)$. The result of this procedure is shown in Fig. 7 for the amorphous $Fe_{39}Tb_{61}$-alloy. The three partial peaks can be associated to the Fe-Fe-, Fe-Tb-, and Tb-Tb-

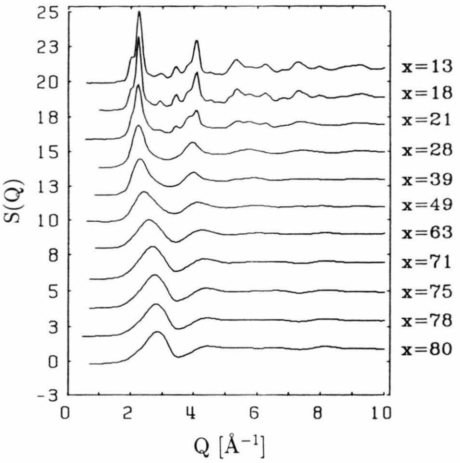

Fig. 5. Amorphous Fe_xTb_{100-x}; $S(Q)$; EDXD-method.

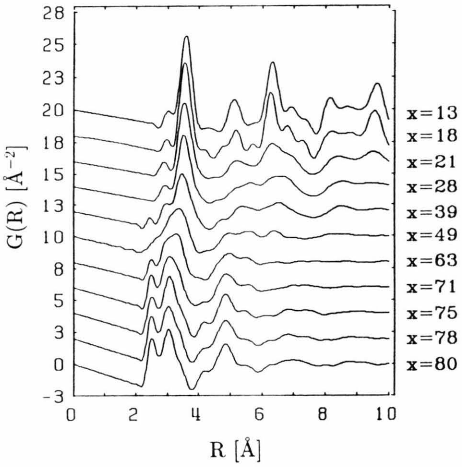

Fig. 6. Amorphous Fe_xTb_{100-x}; $G(R)$; EDXD-method.

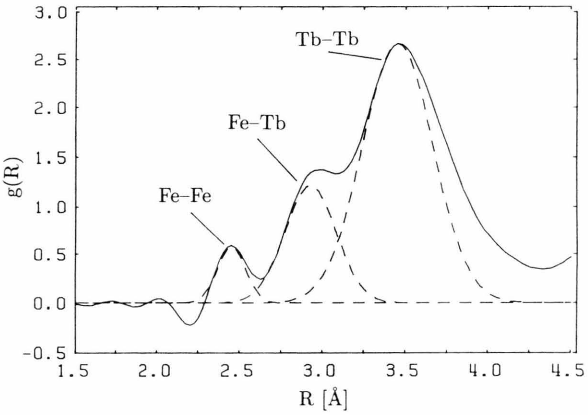

Fig. 7. Amorphous $Fe_{39}Tb_{61}$; Gauss-fit to the $g(R)$ function; EDXD-method.

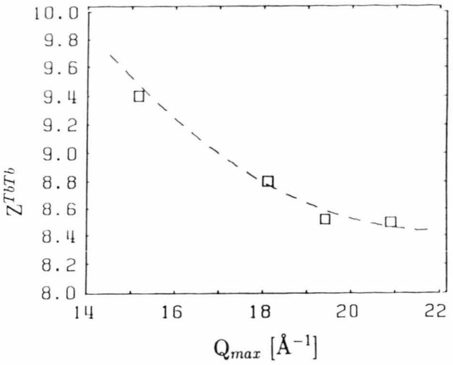

Fig. 8. Amorphous $Fe_{39}Tb_{61}$; partial coordination number Z_{TbTb} versus Q_{max}.

pairs, respectively. Keeping in mind this figure we learn from Fig 6, that for $13 \leqq x \leqq 63$ the Tb-Tb distance dominates the first maximum ($R < 4$ Å), whereas for $x > 71$ the Fe-Tb distance dominates and becomes more and more separated from the Fe-Fe distance. At $x = 49$ the first maximum consists of only one broad peak. It should be mentioned that for this nearly equiatomic composition the weighting-factors W_{TbTb}, W_{FeTb}, and W_{FeFe} amount to 0.5, 0.41, and 0.08, respectively.

Table 2 contains the atomic distances evaluated in the present work. The R_{FeFe}-distances are almost constant and lie between 2.48 and 2.50 Å.

Compared with the shortest Fe-Fe distance of 2.60 Å in crystalline Fe_2Tb, the iron atoms in the amorphous state are closer together. The value of 3.04 Å for R_{FeTb} in crystalline Fe_2Tb corresponds to that observed for the amorphous Fe_xTb_{100-x}-alloys with large x-values. For small x-values R_{FeTb} is below 3 Å. The distance R_{TbTb} in the amorphous alloys was determined to be between 3.41 Å and 3.61 Å and is appreciably larger than the distance in crystalline Fe_2Tb, which amounts to 3.18 Å.

4.1.2.2. Partial Coordination Numbers

Figure 8 shows the partial coordination number Z_{TbTb} versus the maximum Q-value, Q_{max}, used in the Fourier transformation (2). Q_{max} extends from the normally with ADXD accessible maximum Q-value of 14 Å^{-1} up to the Q_{max}-value of 21 Å^{-1} detectable with the EDXD-method. The larger the Q_{max}-value, the more reliable the coordination number.

In Fig. 8 it can be seen that Z_{TbTb} evaluated from EDXD with the highest Q_{max}-value reaches the asymptotic value.

Table 2. Atomic distances R_{FeFe}, R_{FeTb}, and R_{TbTb}.

Specimen	Distances		
	R_{FeFe} [Å]	R_{FeTb} [Å]	R_{TbTb} [Å]
$Fe_{13}Tb_{87}$(SP)	–	3.03	3.58
$Fe_{18}Tb_{82}$(SP)	–	2.98	3.55
$Fe_{21}Tb_{79}$(SP)	–	2.90	3.53
$Fe_{28}Tb_{72}$(SP)	–	2.93	3.52
$Fe_{28}Tb_{72}$(MS)	–	2.85	3.48
$Fe_{39}Tb_{61}$(SP)	2.48	2.93	3.48
$Fe_{40}Tb_{60}$(MS)	2.50	2.95	3.48
$Fe_{49}Tb_{51}$(SP)	2.50	3.01	3.45
$Fe_{63}Tb_{37}$(SP)	2.49	3.00	3.43
cryst. $Fe_{66}Tb_{33}$	2.60	3.04	3.18
$Fe_{71}Tb_{29}$(SP)	2.49	3.03	3.41
$Fe_{75}Tb_{25}$(SP)	2.50	3.05	3.46
$Fe_{78}Tb_{22}$(SP)	2.50	3.02	3.44
$Fe_{80}Tb_{20}$(SP)	2.50	3.03	3.47
$Fe_{68}Co_9Tb_{23}$(SP)	2.48	3.00	3.61
$Fe_{72}Co_8Tb_{20}$(SP)	2.48	2.98	3.43
$Fe_{69}Co_{8.5}Tb_{22.5}$(SP)	2.48	3.05	3.50

Table 3. Partial coordination numbers and short range order parameters.

Specimen	Partial coordination numbers				Short range order parameter
	Z_{FeFe}	Z_{FeTb}	Z_{TbFe}	Z_{TbTb}	η^0_{FeTb}
$Fe_{13}Tb_{87}$(SP)	–	8.1	1.2	10.9	–
$Fe_{18}Tb_{82}$(SP)	–	4.5	1.0	10.5	–
$Fe_{21}Tb_{79}$(SP)	–	5.1	1.4	9.5	–
$Fe_{28}Tb_{72}$(SP)	–	4.8	1.9	9.9	–
$Fe_{28}Tb_{72}$(MS)	–	4.6	1.8	9.1	–
$Fe_{39}Tb_{61}$(SP)	3.7	4.1	2.5	8.5	0.43
$Fe_{40}Tb_{60}$(MS)	3.3	4.2	2.8	9.2	0.46
$Fe_{49}Tb_{51}$(SP)	4.3	5.5	5.3	7.0	0.04
$Fe_{63}Tb_{37}$(SP)	4.2	4.9	8.3	5.4	0.17
cryst. $Fe_{67}Tb_{33}$	6	6	12	4	0.4
$Fe_{71}Tb_{29}$(SP)	5.4	4.5	10.9	3.1	0.42
$Fe_{75}Tb_{25}$(SP)	6.9	4.1	11.8	3.6	0.36
$Fe_{78}Tb_{22}$(SP)	6.6	3.6	12.8	3.3	0.33
$Fe_{80}Tb_{20}$(SP)	7.1	3.4	13.4	3.6	0.31
$Fe_{68}Co_9Tb_{23}$(SP)	8.8	2.6	8.6	7.0	−0.5
$Fe_{72}Co_8Tb_{20}$(SP)	6.6	3.3	13.7	3.5	0.37
$Fe_{69}Co_{8.5}Tb_{22.5}$(SP)	6.9	4.0	12.7	3.2	0.48

Table 3 contains the partial coordination numbers as obtained in the present work with an accuracy of ±10%. Since the influence of the partial G_{FeFe}-function on the total G-function is too small for $x < 39$, no Z_{FeFe}-values could be determined for these alloys.

The specimens produced by sputtering (SP) show an increase of Z_{FeFe} from 3.7 to 7.1 atoms with increasing iron concentration. This is reasonable since high Fe-concentration means also high Fe number density.

The number Z_{FeTb} of Tb-atoms which are arranged around an Fe-atom is about 4, independent from the Fe-concentration, except for the specimen with $x = 13$.

The number Z_{TbFe} of Fe-atoms around a Tb-atom is obtained according to

$$Z_{\mathrm{TbFe}} = \frac{c_{\mathrm{Fe}}}{c_{\mathrm{Tb}}} \cdot Z_{\mathrm{FeTb}} \tag{13}$$

and increases with increasing iron concentration from 1.2 atoms to 13.4 atoms.

Z_{TbTb} decreases with increasing x from 10.9 to 3.6 Tb-atoms around a Tb-atom. This means that with increasing x the Tb-atoms arranged around a Tb-atom are replaced by Fe-atoms. The partial coordination numbers as well as the atomic distances of the melt spun and the sputtered specimens show no significant differences.

Regarding the partial coordination numbers of crystalline $\mathrm{Fe_2Tb}$, Table 3 shows that $Z_{\mathrm{TbTb}} = 4$ corresponds to the average of the values of the neighbouring amorphous phases, whereas the other three partial coordination numbers of the crystalline phase are significantly larger than those of the amorphous phases.

Regarding the previous discussion we conclude that an arrangement of about four Tb-atoms around one Fe-atom seems to be a structure-determining stable configuration for all the amorphous Fe-Tb-alloys. The short range order parameters η^0_{FeTb} calculated according to (10) are shown in Table 3. All $\mathrm{Fe}_x\mathrm{Tb}_{100-x}$-specimens yield a positive CSRO-parameter, which means that there is a more or less pronounced tendency for compound formation.

4.2. Amorphous Fe-Co-Tb-Alloys

Amorphous Fe-Tb- and Fe-Co-Tb-alloys with concentrations of the transition metals larger than about 60 at. % show ferrimagnetic behaviour. The axis of easy magnetization is either perpendicular to the specimen surface or in-plane. For applications in the magneto-optical memory technology the alloys with perpendicular magnetization are used. Table 4 shows the Fe-Co-Tb-alloys investigated in the present paper and their axis of easy magnetization.

Since the atomic diameters of iron and cobalt differ only slightly, the ternary Fe-Co-Tb system is treated as a binary system $\mathrm{TM}_x(\mathrm{RE})_{100-x}$ in the following (TM = Fe, Co; RE = Tb).

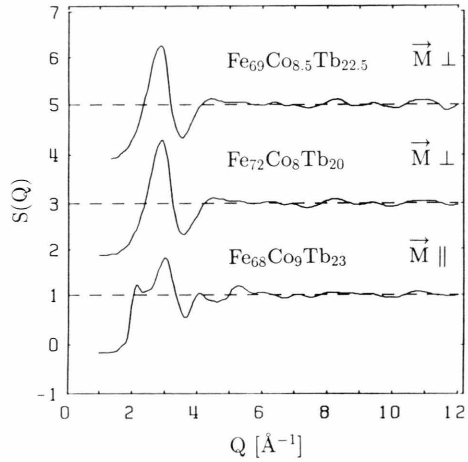

Fig. 9. Amorphous Fe-Co-Tb-alloys; structure factors from EDXD-measurements.

Table 4. Amorphous Fe-Co-Tb-alloys sputtered on Be.

Specimen	Direction of easy axis
$\mathrm{Fe_{72}Co_8Tb_{20}} = (\mathrm{Fe_{0.90}Co_{0.10}})_{80}\mathrm{Tb_{20}}$	perpendicular ($\boldsymbol{M}_\perp$)
$\mathrm{Fe_{69}Co_{8.5}Tb_{22.5}} = (\mathrm{Fe_{0.89}Co_{0.11}})_{77.5}\mathrm{Tb_{22.5}}$	perpendicular ($\boldsymbol{M}_\perp$)
$\mathrm{Fe_{68}Co_9Tb_{23}} = (\mathrm{Fe_{0.88}Co_{0.12}})_{77}\mathrm{Tb_{23}}$	in-plane ($\boldsymbol{M}_\parallel$)

4.2.1. Structure Factors

Fig. 9 shows the total Faber-Ziman structure factors, as obtained with the EDXD-method, for the three alloys listed in Table 4. For reasons of presentation the figure shows only the Q-region up to 12 Å^{-1}. The structure factors for the two specimens with $\boldsymbol{M}_\perp$ are almost identical but they differ from that obtained with the $\boldsymbol{M}_\parallel$-specimen. The main differences are observed at the main maximum, which is split up for amorphous $\mathrm{Fe_{68}Co_9Tb_{23}}$ ($\boldsymbol{M}_\parallel$). This specimen shows two peaks at 2.15 Å^{-1} and 2.99 Å^{-1} whereas the structure factors obtained for $\mathrm{Fe_{72}Co_8Tb_{20}}$ ($\boldsymbol{M}_\perp$) and $\mathrm{Fe_{69}Co_{8.5}Tb_{22.5}}$ ($\boldsymbol{M}_\perp$) show their main peak at 2.9 Å^{-1}.

We note that for the same concentration different orientations of the axis of easy magnetization are possible, which apparently are correlated with the differences in $S(Q)$ (see Figure 9).

Table 5. Amorphous Fe-Co-Tb-alloys, amorphous $Fe_{79}Tb_{21}$, and $Co_{82}Gd_{18}$; atomic distances and partial coordination numbers.

	$\boldsymbol{M}_{\parallel}$ $Fe_{68}Co_9Tb_{23}$	$\boldsymbol{M}_{\perp}$ $Fe_{72}Co_8Tb_{20}$	$\boldsymbol{M}_{\perp}$ $Fe_{69}Co_{8.5}Tb_{22.5}$	$Fe_{78}Tb_{22}$ (Tables 2, 3)	$Co_{82}Gd_{18}$ [11]
$R_{\mathrm{TM\,TM}}$ [Å]	2.48	2.48	2.48	2.50	2.47
$Z_{\mathrm{TM\,TM}}$	8.8	6.6	6.9	6.6	7.2
$R_{\mathrm{TM\,RE}}$ [Å]	3.00	2.98	3.05	3.02	2.97
$Z_{\mathrm{TM\,RE}}$	2.6	3.3	4.0	3.6	–
$Z_{\mathrm{RE\,TM}}$	8.6	13.7	12.7	12.8	–
$R_{\mathrm{RE\,RE}}$ [Å]	3.61	3.43	3.50	3.44	3.4
$Z_{\mathrm{RE\,RE}}$	7.0	3.5	3.2	3.3	3

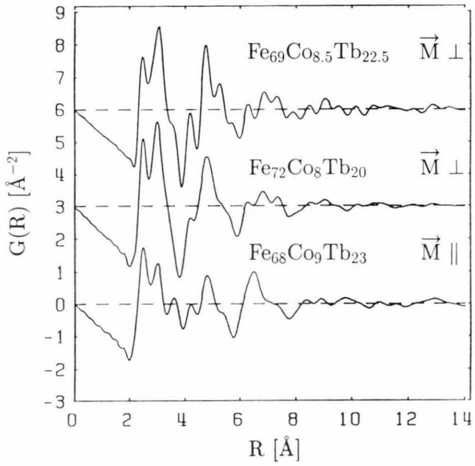

Fig. 10. Amorphous Fe-Co-Tb-alloys; pair correlation functions from EDXD-measurements.

4.2.2. Pair Correlation Functions

The Fourier transforms of the structure factors in Fig. 9, i.e. the total pair correlation functions are presented in Figure 10. In all cases no pronounced correlations exist for $R > 8$ Å. From the two upper $G(R)$-curves the lower one shows less pronounced correlations in the region of the second maximum between 3.8 Å and 5.8 Å and in the region of the third maximum between 5.8 Å and 8 Å. In the region of the first coordination sphere the two upper curves ($\boldsymbol{M}_{\perp}$) are split up only into two peaks, whereas the lowest ($\boldsymbol{M}_{\parallel}$) curve is split up into three peaks. Table 5 contains the atomic distances and partial coordination numbers as obtained from Fig. 10 using the method of Gaussian fitting to the corresponding $g(R)$-function.

The atomic distances $R_{\mathrm{TM\,TM}}$ and $R_{\mathrm{TM\,RE}}$ correspond to the sum of the atomic radii (Fe: 1.24 Å; Tb: 1.76 Å), i.e., each atom is in direct contact with the surrounding atoms. The atomic distance $R_{\mathrm{RE\,RE}}$ is largest for the $Fe_{68}Co_9Tb_{23}$-alloy ($\boldsymbol{M}_{\parallel}$) and appears in Fig. 10 as a separate peak. The partial coordination numbers of the $\boldsymbol{M}_{\parallel}$- and $\boldsymbol{M}_{\perp}$-specimens are totally different.

Table 5 also contains the data for the amorphous $Fe_{78}Tb_{22}$- and $Co_{82}Gd_{18}$-alloys as obtained in the present paper and in [11]. Both alloys show almost the same distances and partial coordination numbers as the Fe-Co-Tb-alloys with $\boldsymbol{M}_{\perp}$.

We have already presented in Table 2 the chemical short range order parameters for the amorphous Fe-Co-Tb-alloys as obtained from the partial coordination numbers in Table 5. The normalized short range order parameter η^0_{FeTb} is negative for amorphous $Fe_{68}Co_9Tb_{23}$ ($\boldsymbol{M}_{\parallel}$). This is the first example for an amorphous substance showing a negative η^0_{FeTb}-value. This means segregation tendency, i.e. formation of (Fe-Co)- and/or (Tb-H)-clusters (see below). A correlation is suggested between this result and the observation of X-ray small angle scattering with this alloy [12]. For both $\boldsymbol{M}_{\perp}$-specimens η^0_{FeTb} is positive, which means compound formation, i.e. the Tb-atoms preferentially are surrounded by Fe-atoms and vice versa.

As shown in 4.2.1 the amorphous $Fe_{68}Co_9Tb_{23}$ ($\boldsymbol{M}_{\parallel}$)-alloy differs in its atomic structure from the $Fe_{72}Co_8Tb_{20}$ ($\boldsymbol{M}_{\perp}$)- as well as from the $Fe_{69}Co_{8.5}Tb_{22.5}$ ($\boldsymbol{M}_{\perp}$)-alloy. In the following we discuss, whether these structural differences point to a structural anisotropy which could cause a magnetic anisotropy. A measure for the structural anisotropy is given by the so-called anisotropic structure factor $\Delta S(Q)$ [13]:

$$\Delta S(Q) = S(Q_{\parallel}) - S(Q_{\perp}) \tag{14}$$

with

$S(Q_{\parallel})$ = structure factor obtained in a transmission experiment, where Q lies in the specimen plane,

$S(Q_{\perp})$ = structure factor obtained in a reflexion experiment, where Q is perpendicular to the specimen plane.

The structural anisotropy is expected to be very small. The high counting rate in EDXD-measurements minimizes the error from counting statistics compared to ADXD-measurements. Thus small changes in the experimental spectra can be determined with high accuracy. Nevertheless the experimental results showed $\Delta S(Q)$ to be zero. It was pointed out in [14] that the preferred orientation of only 1% of the atomic pairs is sufficient to explain the magnetic anisotropy. Thus with the present amorphous Fe-Co-Tb-alloys the magnetic anisotropy could be caused by such a small structural anisotropy which could not even be detected with the EDXD-method.

From neutron diffraction experiments with the Fe-Co-Tb-alloys it was concluded that the $Fe_{68}Co_9Tb_{23}$ ($\boldsymbol{M}_{\parallel}$)-alloy contains about 10 at.% hydrogen [15]. This hydrogen content is brought into the production process from the sputtering target. We suppose that this hydrogen content stimulates the segregation tendency and furthermore is responsible for the ($\boldsymbol{M}_{\parallel}$)-anisotropy. The larger Tb-Tb-distance in the $\boldsymbol{M}_{\parallel}$-specimen compared to those in the $\boldsymbol{M}_{\perp}$-specimens, whereas $R_{\mathrm{TM\,TM}}$ and $R_{\mathrm{TM\,RE}}$ are about the same, shows that the hydrogen is embedded preferentially into Tb-rich regions. If this process would alter the resulting magnetic moment of the Tb-atoms then the anisotropy could be explained in a similar way as it was done with amorphous Gd-Co-alloys with inserted oxygen [16].

Acknowledgements

Thanks are due to Deutsche Forschungsgemeinschaft, Bad Godesberg, for financial support of this work.

[1] B. C. Giessen and G. E. Gordon, Science **159,** 973 (1968).
[2] J. M. Prober and J. M. Schultz, J. Appl. Cryst. **8,** 405 (1975).
[3] T. Egami, J. Mat. Science **13,** 2587 (1978).
[4] G. A. N. Connell, J. Magn. Magnetic Materials **54–57,** 1561 (1986).
[5] N. Imamura, S. Tanaka, F. Tanaka, and Y. Nagao, IEEE Trans. Magn. MAG-**21 (5),** 1607 (1985).
[6] T. E. Faber and J. M. Ziman, Phil. Mag. **11,** 153 (1965).
[7] G. S. Cargill and F. Spaepen, J. Non-Cryst. Solids **43,** 91 (1981).
[8] R. Utz, doctor thesis, University of Stuttgart 1989.
[9] F. Burgäzy and M. Dudek from this Institute, personal communication.
[10] P. Lamparter, W. Sperl, E. Nold, G. Rainer-Harbach, and S. Steeb, Proc. 4th Int. Conf. on Rapidly Quenched Metals, Sendai 1982, p. 343.
[11] G. S. Cargill III, Solid State Phys. **30,** 227 (1975).
[12] H. Träuble from this Institute, personal communication.
[13] Y. Suzuki, J. Haimovich, and T. Egami, Phys. Rev. **B 35 (5),** 1083 (1987).
[14] G. S. Cargill III, AIP Conf. Proc. **24,** 138 (1975).
[15] M. Heckele from this Institute, personal communication.
[16] A. Brunsch and J. Schneider, IEEE Trans. Magn. MAG-**13 (5),** 1606 (1977).